ANNALS OF GEOPHYSICS, 69, 2, SA221, 2026; doi:10.4401/ag-9468
OPEN ACCESS

Ionospheric foF2 Prediction Using an Interpretable XGBoost Model and COSMIC-1 and 2 Radio Occultation Data

Fen Wang[1], Ming Ou[*,2], QingLin Zhu[1], JingJing Li[1], Qiang Zhang[3], YuHang Zhang[1], LongJiang Chen[1], XiaoRui Chong[4]

(1) China Research Institute of Radiowave Propagation, Qing Dao, China
(2) Department of Ocean Science and Engineering, Shandong University of Science and Technology, Qing Dao, China
(3) Xidian University, Department of Physics, Xi An, China
(4) Shandong University of Science and Technology, Department of Electronic and Information Engineering, Qing Dao, China

Article history: received October 29, 2025; accepted April 26, 2026

Abstract

The critical frequency foF2 of the ionosphere's F2 layer plays a key role in shortwave communications. Its variability is influenced by factors such as solar activity and geomagnetic conditions, making accurate prediction of foF2 essential for reliable communication in navigation, aviation, and emergency scenarios. This paper presents a global foF2 prediction model based on occultation data from 2007 to 2023 and the eXtreme Gradient Boosting (XGBoost) algorithm. The model incorporates the SHAP method for interpretability analysis, which identifies the core factors driving its predictions. The results show a coefficient of determination (R^2) of 0.886 and a root mean square error (RMSE) of 0.964 MHz on the test set. The model captures key ionospheric features, including the single peak at the magnetic equator, the double peak of the equatorial anomaly, the Weddell Sea anomaly, and the winter anomaly. Verification with independent datasets from the GRACE satellite and GIRO radiosonde demonstrates that the model outperforms the IRI-2020, NPDM, and random forest (RF) models, achieving the highest R^2 and reducing errors by over 50% at mid- and high-latitudes. When COSMIC-2 data were added, the model's performance improved, with a 2.39% reduction in mean absolute error (MAE) and a 2.63% reduction in RMSE for latitudes between –42.55° and 42.91°. SHAP analysis highlighted the core driving factors of the model, including latitude, time of day, annual cumulative day, F10.7 index, and longitude. Feature ablation experiments revealed that only six features were needed to achieve core accuracy, with an R^2 greater than 0.85 and a ΔR^2 of –0.038.

Keywords: COSMIC; Global foF2 Forecast; Machine Learning; SHAP; Radio Occultation

1. Introduction

Accurate prediction of ionospheric parameters is crucial for both national defense and civilian applications such as satellite navigation, ground-based radar, and shortwave communication (Forsythe, 2024). The ionosphere, situated between the neutral lower atmosphere and the plasma-dominated outer space, is uniquely influenced by both the dynamic processes of the lower atmosphere and solar activity. As the region with the peak electron density, the F2 layer is essential for long-distance shortwave communications due to its high ionization (Wang, 2023). The critical frequency (foF2) of the ionospheric F2 layer is defined as the highest frequency at which vertically incident electromagnetic waves can be reflected. Waves with frequencies above foF2 will penetrate the ionosphere, disrupting long-distance communication (Pezzopane, 2007). Therefore, precise prediction of foF2 is vital to the stable operation of high-frequency radar, shortwave communications, and related systems (Li, 2021; Qiao, 2024).

Traditional ionospheric models are primarily based on empirical formulas or physical equations. For instance, the Klobuchar model has been improved for better GNSS ionospheric delay correction (Wang, 2016). The IRI model is stable under calm space conditions but fails to account for extreme space weather events and regional variations (Forsythe, 2024). Physics-based models such as TIE-GCM provide detailed ionospheric predictions but are difficult to implement in real time (Qian, 2014).

In recent years, artificial intelligence has been widely used in ionospheric research. Neural networks were early applied for ionospheric modeling (Habarulema, 2009). Li et al. (2021) developed a deep learning model to predict foF2 in East Asia. Bi et al. (2022) modeled foF2 variations in low-latitude regions during different solar activity years. Shi et al. (2025) proposed a hybrid deep learning model for short-term foF2 forecasting. Qiao et al. (2024) developed an ionospheric foF2 model using the Informer network for long time-series prediction. Zewdie et al. (2021) applied random forest and LSTM for low-latitude TEC forecasting.

XGBoost has shown excellent performance in ionospheric research (Lin, 2021; Zhao, 2023). Chen and Guestrin (2016) proposed the XGBoost algorithm as a scalable tree boosting system. To address the black-box problem of machine learning, the SHAP method was proposed for model interpretation (Lundberg and Lee, 2017). TreeSHAP was further developed for tree-based models (Lundberg et al., 2018a). SHAP has been successfully applied in many fields (Lundberg et al., 2018b; Cohen, 2024).

In this study, IRI-2020 and NPDM are used as climatological and empirical baseline models, while XGmodel and RF are employed as data-driven machine learning models for performance comparison.

2. DATA Set construction

2.1 foF2 data extraction

COSMIC-1, COSMIC-2, and GRACE served as the primary sources of occultation data for this study. COSMIC-1 records nearly 2,500 electron density profiles daily (reducing to 1,000-1,500 after 2011), totaling 4.5 million profiles over a solar cycle. These profiles, spanning high, mid, and low latitudes worldwide, offer high vertical resolution, making them ideal for studying ionospheric variability and modeling. In contrast, COSMIC-2 primarily targets tropical and subtropical regions, but it records approximately 5,000 occultation events daily. Additionally, COSMIC-2's ability to receive dual-frequency signals from both GPS and GLONASS enhances its data coverage.

GRACE satellite data provided independent verification, with the GRACE-A and GRACE-B systems operating from 2002 to 2017. These satellites continuously collected ionospheric occultation observations worldwide, particularly in polar regions and mid- to high-latitudes, where COSMIC-1/2 coverage is limited. Over one and a half solar cycles, they accumulated more than one million high-quality global ionospheric profiles. Although GRACE offers fewer daily electron density profiles (approximately 200) compared to the COSMIC series, its long-term, stable observations are invaluable for studying the global distribution, solar cycle dependence, and seasonal variability of foF2. The high vertical resolution of GRACE data accurately captures the height (hmF2) and shape of the F2 layer peak, ensuring precise inversion of foF2 and facilitating research into its physical mechanisms. Additionally, the use of high-precision intersatellite link technology guarantees the reliability and consistency of the observational data.

The GIRO vertical instrument is a key independent data source for ionospheric research. Although it provides single-point observations, its long-term monitoring has generated a substantial dataset. It accurately measures both foF2 and hmF2, and its data, spanning multiple solar cycles, are invaluable for F2 layer research. With high accuracy,

reliability, and consistency, GIRO data provide a solid foundation for understanding the physical mechanisms of the ionosphere.

COSMIC and GRACE data are available from CDAAC (https://data.cosmic.ucar.edu/gnss-ro), while GIRO data can be downloaded in batches from https://lgdc.uml.edu. After downloading the GIRO automated interpretation data, foF2 values can be directly extracted, cleaned, and compiled into a dataset.

2.2 Obtaining the Solar Activity Index and Geomagnetic Activity Index

In addition to occultation and ionosonde data, we also require solar and geomagnetic activity data from 2007 to 2023, along with electron density profiles. Solar and geomagnetic activity data for this study were sourced from multiple authoritative providers, covering the period from 2007 to 2023. These data include key parameters such as Kp, Ap, F10.7, Dst, Vsw and SSN, available at https://omniweb.gsfc.nasa.gov/form/dx1.html. The Ap index is a daily average of magnetic field activity, calculated from the Kp index, and measures short-term (one-day) geomagnetic disturbances. F10.7 represents the intensity of 10.7 cm solar radiation and is a key indicator of solar activity. The Dst index quantifies disturbances in the horizontal component of the geomagnetic field in the equatorial region. Vsw refers to the speed of the solar wind, which is the velocity of plasma emitted by the sun. SSN measures the number of sunspots, reflecting solar activity levels.

To ensure data accuracy, outliers and missing values must be analyzed and corrected. The Isolation Forest algorithm detects outliers by isolating data points. It is efficient, scalable, does not require assumptions about data distribution, can handle high-dimensional data, and is robust [22]. This algorithm is applied to identify outliers, with the outlier ratio set to 0.0001 to minimize the impact of excessive interpolated values. Invalid data (represented by 9999) is marked as NAN, and linear interpolation is then used to fill in the missing values. This approach addresses the issue of insufficient valid data in the sliding window, preventing NAN values from hindering effective data processing. The data processing flowchart is shown in Fig. 1.

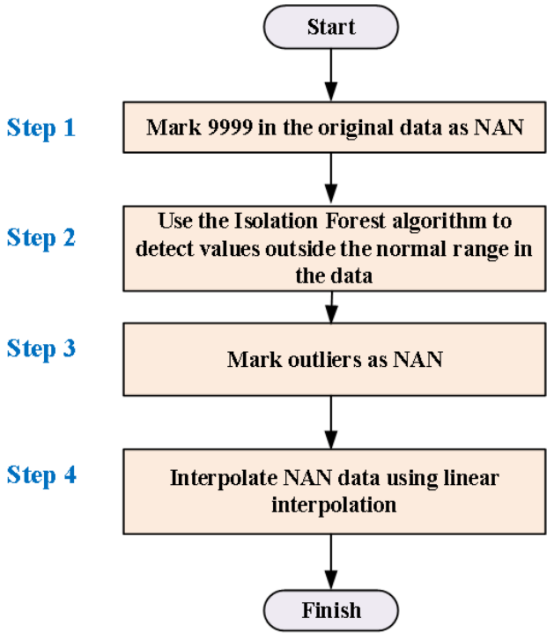

Figure 1. Data cleaning flow chart.

Several factors, such as solar activity and plasma irregularities, can impact the accuracy and precision of electron density inversions from occultations (Joseph, 2015). These factors may cause significant fluctuations in the inverted electron density profile or result in a lack of a clear peak, leading to deviations from the true electron density. Therefore, before further analysis or application, occultation data must be screened to eliminate invalid electron density profiles. In this paper, a valid foF2 is obtained through the following five steps (Han, 2024).

The peak height of the F2 layer in the COSMIC occultation ionospheric data is defined as a valid electron density profile within the following range:

$$150 \text{ km} < h_mF_2 < 500 \text{ km} \tag{1}$$

Among them, h_mF_2 is the height corresponding to the peak electron density of the F2 layer of the ionosphere, that is, the peak height.

After obtaining the peak height, the corresponding electron density at this height is calculated to determine the foF2 value. The calculation formula is as follows.

$$foF2 = \sqrt{80.6NmF2} \tag{2}$$

The critical frequency of the F2 layer in the ionospheric data of COSMIC occultation observations is set in the following range:

$$0.1 \text{ MHz} \leq foF \leq 22 \text{ MHz} \tag{3}$$

Define it as electron density gradient and set the range as follows:

$$-9 < S = \frac{Ne_{high} - Ne_{low}}{H_{high} - H_{low}} \times \frac{1}{1000} < -0.02 \tag{4}$$

where H_{low} and H_{high} are the lowest and highest altitudes, Ne_{low} and Ne_{high} are the corresponding electron densities at the lowest and highest altitudes, respectively.

The following definitions are used to screen the acquired COSMIC occultation observation ionospheric data:

$$\sum_i \frac{\left|Ne_i - \overline{Ne_i}\right|}{N\overline{Ne_i}} \leq 1.5 \tag{5}$$

Among them, Ne_i is the original electron density, $\overline{Ne_i}$ is the electron density after the original electron density is sliding averaged over 9 windows, and N is the total electron density.

At the same time, the selection of the Ne profile is constrained during the processing so that the horizontal difference is within 5° to eliminate the influence of the horizontal difference on the results. The formula is set as follows:

$$\begin{cases} \Delta\theta = arctan\left(\dfrac{\Delta h}{\Delta Ne}\right) \\ \Delta\theta \leq 5^\circ \end{cases} \tag{6}$$

Where, Δh is the horizontal distance and ΔNe is the electron density change at adjacent heights.

The electron density profile is the effective electron density profile after being processed by the above steps. Finally, the foF2 data is extracted.

2.3 Dataset Construction

After data quality control, the features and data format of the final dataset are shown in the following Table1:

Table 1. Main training parameters of the dataset and their meanings.

Serial number	Feature	Feature meaning
1	Year	Year
2	Month	Month
3	Day	Day
4	Doy	Day of year
5	UT	Universal Time
6	LT	Local Time
7	Lat	Latitude
8	Lon	Longitude
9	Kp	Magnetic field activity index
10	Ap	Daily average magnetic field activity index
11	F10.7	Solar activity index
12	Dst	Geomagnetic index
13	Vsw	Solar wind speed
14	SSN	Sunspot number
15	UT*Lon	Combined features
16	Dst*lat	Combined features

After data cleaning, the solar and geomagnetic activity indices effectively eliminate outliers and fill in missing values, ensuring the data remains within normal ranges. The distributions of the F10.7 (Fig. 2a) and SSN (Fig. 2b) indices after cleaning are presented in the following figures. As shown, all values fall within the normal range. Due to missing data from the COSMIC satellite between April 25, 2020, and January 6, 2021, no data is available for this period in the figure.

A feature dataset is built using the cleaned data, with combined features UT*Lon and Dst*Lat created to capture spatiotemporal coupling effects. This approach enhances the model's ability to learn complex geographic and temporal distributions, improving its understanding of how solar and geomagnetic activity impacts different regions. By incorporating these features, the model's expressive power is increased, enabling it to more effectively extract valuable information from spatiotemporal dimensions.

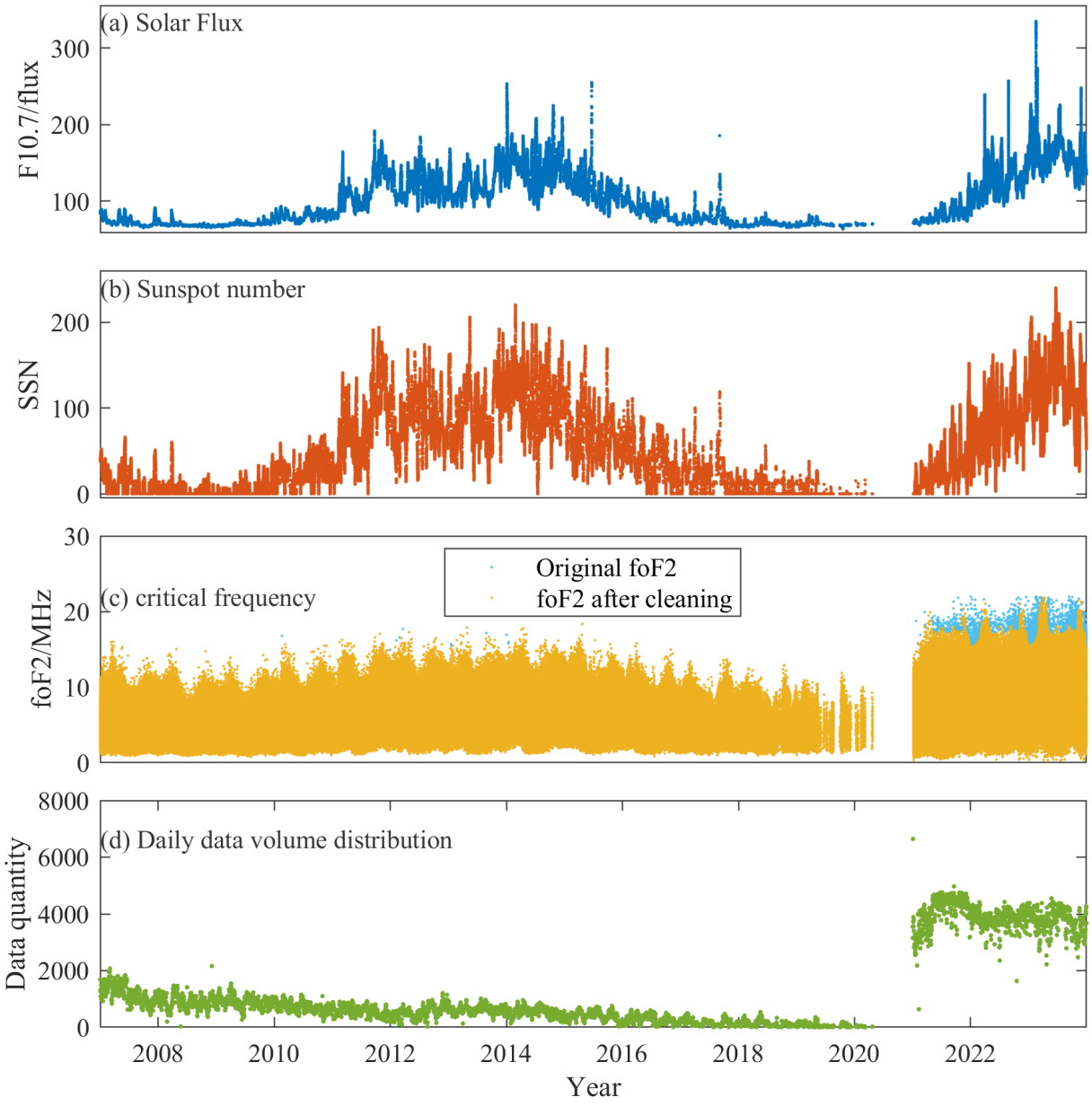

Figure 2. F10.7 (a), SSN (b), foF2 (c). Distribution diagram of effective data volume of the dataset every day (d).

The dataset is divided by year, with data from 2014 and 2019 used as independent test sets to validate the model's temporal generalization capabilities, while data from other years is used for training. By selecting 2014, a year of high solar activity, and 2019, a year of low solar activity, as test sets, we can effectively evaluate the model's extrapolation and prediction abilities in extreme space environments. The training set includes data from years with moderate solar activity to ensure the model fully captures the evolution of the solar activity cycle. During training, all features and target variables are normalized to the range [0, 1].

To assess the generalization ability of the XGmodel, this study used external GRACE satellite data from 2014 and measurement data from seven GIRO stations in 2019 as benchmarks. The GRACE electron density data was processed to calculate the foF2 value, which was then used to evaluate the model's prediction accuracy. Additionally, to test the model's interpretability, 50% of the GRACE dataset was randomly selected as the background, and SHAP values were calculated for the remaining samples.

All the data used in this paper are shown in Table 2.

Table 2. The total data size, data source, time span, SHAP calculation sample data volume, and number of GIRO stations in the training set, test set, and validation set of this study.

Dataset	Total data size	Data source	Time span	SHAP calculates the number of data samples	Number of stations
Training set	6,587,430	COSMIC	2007-2013 2015-2018 2020-2023	10,000	—
Test set	218,018	COSMIC	2014, 2019	—	—
Validation set	15,425	GRACE	2014	3,000	—
	54,030	GIRO	2019	—	7

3. Modeling and Model Interpretability Analysis

3.1 Modeling Algorithm and Parameter Tuning Method Selection

The experimental results compare the performance between the climatological baseline models (IRI-2020, NPDM) and the data-driven machine learning models (XGmodel, RF).

Random forest is a powerful, versatile, and user-friendly machine learning algorithm. It builds multiple distinct decision trees using bagging and feature randomness and achieves more accurate and stable predictions by combining the results through collective voting (Breiman, 2001).

XGBoost is a boosting algorithm derived from Gradient Boosting Decision Trees (GBDT). Known for its efficiency, flexibility, and accuracy, it is widely used in classification and regression tasks (Chen, 2016). XGBoost, or eXtreme Gradient Boosting, improves upon GBDT by optimizing the loss function through a series of weak learners. The core idea is to train a new weak learner in each iteration to correct the errors of the previous model. The final prediction model is a powerful combination of all these weak learners.

XGBoost uses a second-order Taylor expansion, and its loss function ς for the predicted value $\hat{y}$ can be expressed as a second-order Taylor expansion [25]:

$$\varsigma(y, \hat{y} + \delta) \approx \varsigma(y, \hat{y}) + g\delta + \frac{1}{2}h\delta \tag{7}$$

Among them, g is the gradient of the loss function with respect to the predicted value, h is the second-order derivative of the loss function, that is, the Hessian matrix.

We built an RF model using the random forest algorithm to predict foF2, achieving an RMSE of 1.549 MHz and an R^2 of 0.769 on the test set. In contrast, the final optimized XGBoost model achieved an RMSE of 0.964 MHz and an R^2 of 0.886 on the independent test set. Based on these results, we selected XGBoost for foF2 prediction modeling.

This paper employs the XGBoost regression framework with a Bayesian optimization strategy to search the hyperparameter space. RandomizedSearchCV is used for 5-fold cross-validation, with RMSE as the evaluation metric. A total of 100 parameter combinations are randomly sampled, and an early stopping mechanism is implemented to prevent overfitting. The hyperparameter combination yielding the best performance on the validation set is selected for model building. The XGBoost algorithm predicts foF2 by using an ensemble of decision trees, where each tree is trained sequentially based on the input features, ω_1, $\omega_2 \ldots \omega_n$. The first tree provides an initial prediction, and each subsequent tree corrects the errors of the previous one. The final prediction is the combined result of all trees, leading to a more accurate forecast of foF2. The prediction framework of the XGBoost model is illustrated in Fig. 3.

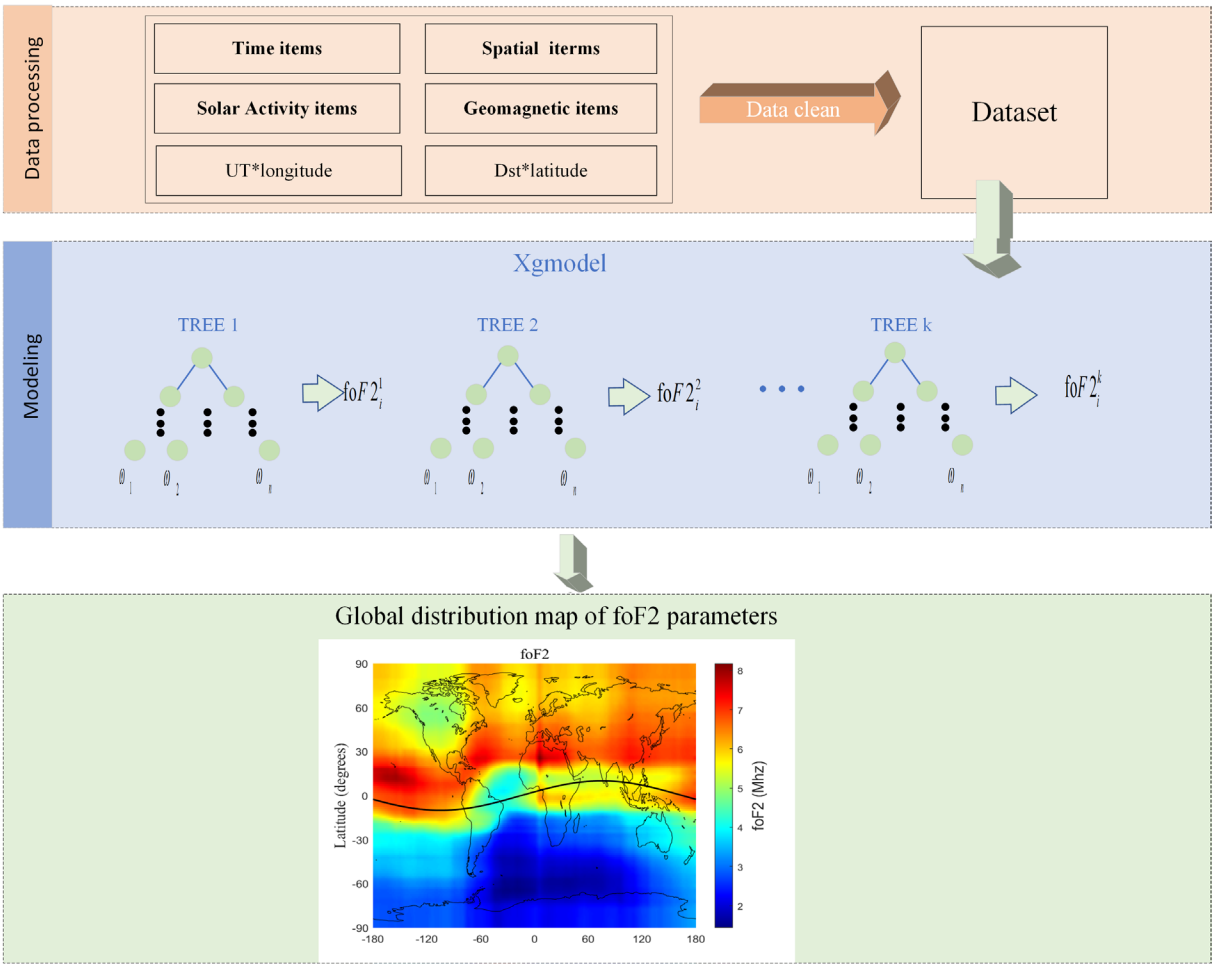

Figure 3. Schematic diagram of the interpretable XGmodel framework.

RMSE effectively captures the impact of extreme values and accurately reflects the magnitude of prediction errors, making it particularly suitable for ionospheric parameters with significant spatial variations. The coefficient of determination (R^2) measures the degree of linear correlation between predicted and observed values. MAE provides an intuitive indication of the average difference between predicted and observed values. The calculation formulas for these metrics are shown in Eq. (8), Eq. (9) and Eq. (10).

$$RMSE = \sqrt{\frac{1}{N}\sum_{i=1}^{N}\left(foF2_{\text{obs}} - foF2_{\text{pre}}\right)^2} \tag{8}$$

$$R^2 = 1 - \frac{\sum_{i=1}^{N}\left(foF2_{\text{pre}}^{i} - foF2_{\text{obs}}\right)^2}{\sum_{i=1}^{N}\left(foF2_{\text{obs}}^{i} - \overline{foF2_{\text{obs}}}\right)^2} \tag{9}$$

$$MAE = \frac{1}{N}\left|foF2_{\text{obs}} - foF2_{\text{pre}}\right| \tag{10}$$

$foF2_{obs}$: $foF2$ observations
$foF2_{pre}$: $foF2$ predicted value
N:Total data of $foF2$

XGBoost offers strong performance, but its effectiveness depends heavily on the proper tuning of hyperparameters. Incorrect settings can lead to overfitting, underfitting, or inefficient training. Therefore, systematic parameter tuning is crucial when using XGBoost. To prevent overfitting, Bayesian optimization with Optuna is used, along with 5-fold cross-validation (KFold), which increases computational costs. Alternatively, random search samples hyperparameter combinations randomly and can sometimes find effective configurations more quickly.

The model optimized with Bayesian optimization achieved an RMSE of 0.957 MHz and an R^2 of 0.864, while the model optimized with random search achieved an RMSE of 0.928 MHz and an R^2 of 0.868. Based on these results, random search was selected as the preferred hyperparameter tuning method.

3.2 SHAP

SHAP considers each feature as a participant in the model prediction process. The SHAP value of each feature reflects its contribution to the prediction result in different feature combinations. By weighted averaging to eliminate the influence of feature order, the final SHAP value that conforms to Shapley's fair distribution axiom is obtained [18]. Its mathematical expression is shown in Eq. (3-5) [17]. The sum of the SHAP values of all features is equal to the difference between the model prediction and the baseline value, as shown in Eq. (11).

$$\phi_i(v) = \sum_{S \subseteq N \setminus \{i\}} \frac{|S|!\,(n - |S| - 1)!}{n!} [v(S \cup \{i\}) - v(S)] \tag{11}$$

N: The set of all features, totaling n;
S: The subset that does not contain feature i;
$v(S)$: Model output value for subset S;
$v(S \cup \{i\})$: Model output value after including feature i;
weight item $\frac{|S|!\,(n - |S| - 1)!}{n!}$: Assign weights based on subset size to ensure fairness.

$$\mathrm{c}\sum_{\mathrm{i}=1}^{n} \phi i = foF2_{pre} - E\left[foF2_{pre}\right] \tag{12}$$

4. Model evaluation

4.1 Analysis of model prediction results

The sunspot number (SSN) reflects the level of solar activity. As shown in Fig. 2b, 2014 was a year of high solar activity, while 2019 was a year of low solar activity. These two years were used as independent test sets.

After splitting the dataset into training and test sets, we used the training set to build a model, which was then applied to predict the 218,018 data points in the test set. The predicted values were compared to the observed values, and the results were visualized in a density scatter plot (Fig. 4). The color bar indicates data density. With an R^2 of 0.886, the model shows a strong correlation between predicted and observed values, indicating a good overall fit. The RMSE is 0.964 MHz. The horizontal axis represents the observed values, and the vertical axis represents the predicted values. High-density areas are concentrated in the 2-8 MHz range, reflecting the model's stable prediction of typical foF2 values.

At night, the ionosphere's electron density typically decreases due to the loss of solar radiation, resulting in a reduction of foF2. However, in the Weddell Sea region, foF2 is higher at night during summer than in the daytime, contrary to the global trend. In contrast, the winter anomaly in mid-latitudes is characterized by higher foF2 values during the winter day compared to the summer day (Gowtam, 2017).

To compare the diurnal variations of the Weddell Sea anomaly with the winter anomaly, this study focused on days 14 and 197 of 2014. Day 180 was selected as a benchmark because solar radiation is stable during this period,

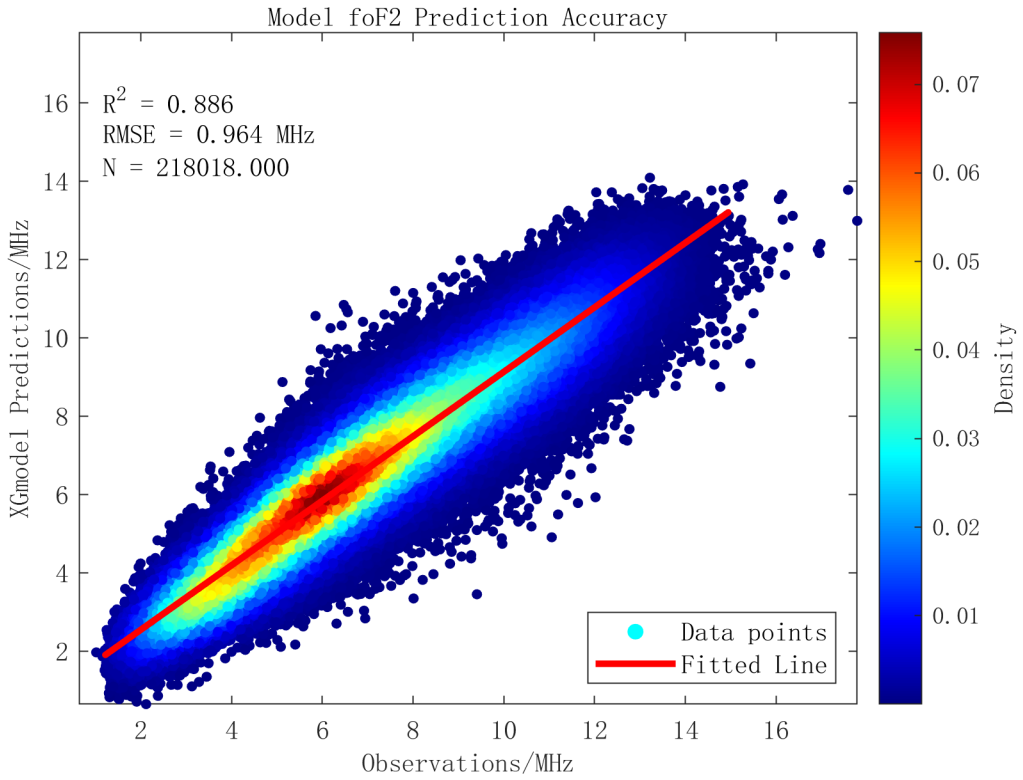

Figure 4. XGmodel prediction test set foF2 density scatter plot.

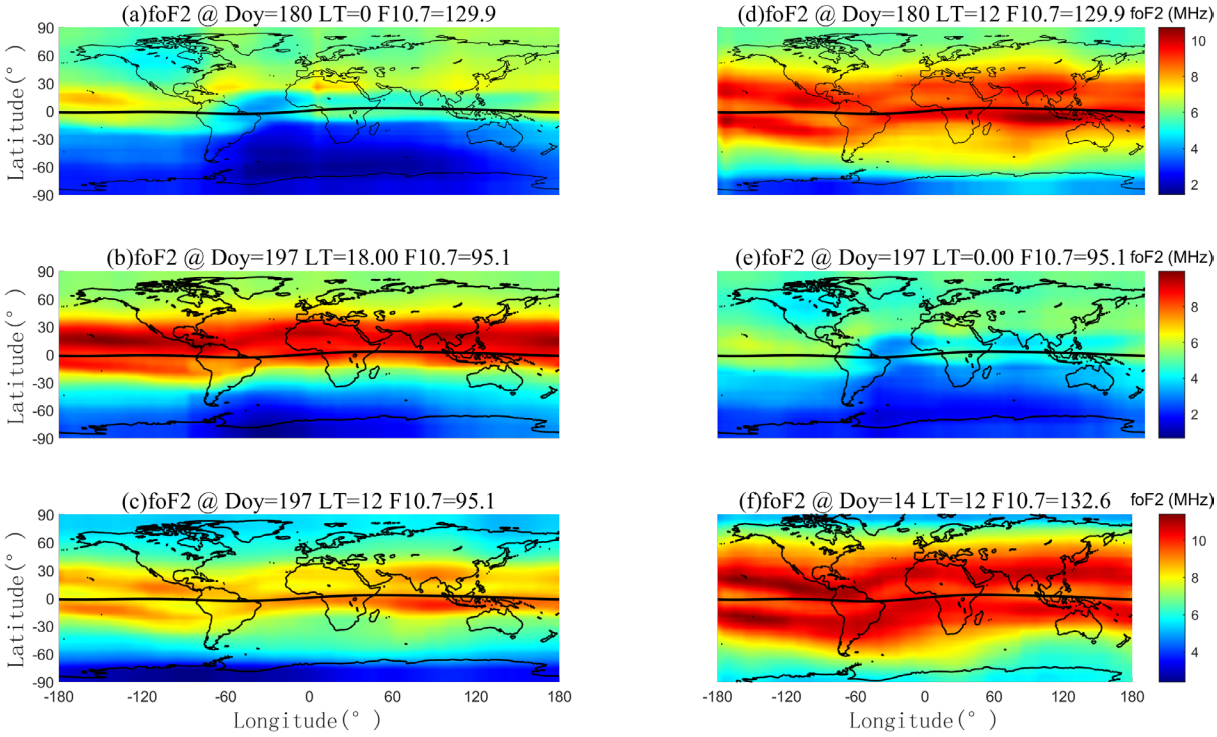

Figure 5. XGmodel predicts the global distribution of foF2 at different times and seasons: Fig. 5a successfully reproduces the unimodal distribution of foF2 near the magnetic equator; Fig. 5d accurately presents the bimodal structure of the equatorial anomaly at approximately ±15° latitude on both sides of the magnetic equator; Fig. 5b and Fig. 5e show that foF2 in the Antarctic region is significantly higher at local time during summer nights at 0:00 than at local time at 18:00; Fig. 5c and Fig. 5f clearly show that foF2 in mid-latitude regions at noon in winter is significantly higher than at noon in summer.

providing an ideal reference for verifying the model's ability to replicate the standard morphology of the equatorial ionosphere.

The model predictions, shown in Fig. 5, depict foF2 values using a color scale where blue indicates lower values and red indicates higher values. Figure 5a accurately reproduces the single-peak foF2 distribution near the magnetic equator at LT = 0. Figure 5d successfully replicates the double-peak structure of the equatorial anomaly at approximately ±15° latitude on either side of the magnetic equator at LT = 12.

In Figs. 5b and 5e, the color at LT = 0 in the Antarctic region is notably lighter than at LT = 18, indicating that foF2 at night during summer is higher than during the day, which confirms the model's accurate representation of the Weddell Sea anomaly. Furthermore, in Figs. 5e and 5f, the mid-latitude region in Fig. 5f appears darker at LT = 12, showing that foF2 during the winter daytime is significantly higher than during the summer daytime, validating the model's reproduction of the winter anomaly.

4.2 Comparative Analysis of Prediction Accuracy between XGmodel and Random Forest RF, IRI-2020, and NPDM Models

It should be emphasized that IRI-2020 and NPDM are climatological baseline models, which are constructed based on long-term statistical averages and mainly used to describe the monthly or seasonal climatological variation of ionospheric parameters. These models are not designed to capture short-term fluctuations driven by sudden solar activity and geomagnetic storms. In contrast, XGmodel and RF are data-driven machine learning models, which can learn and predict instantaneous and spatiotemporal variation of foF2. Therefore, the comparison between XGmodel and IRI/NPDM mainly highlights the ability of machine learning models to capture short-term ionospheric variability, while the comparison between XGmodel and RF provides a fair evaluation of the performance of different data-driven methods.

The International Reference Ionosphere (IRI) model is a global ionospheric model that provides monthly average predictions of ionospheric parameters at various altitudes and geographic locations (Bilitza, 2017). Developed through international research collaboration, the IRI model aims to standardize ionospheric data for applications such as radio communication, satellite navigation, and space weather forecasting (Vesnin, 2015). This study employs the CCIR coefficient from the IRI-2020 model, activating the storm mode to simulate storm deviations. The Eq. (13), Eq. (14) and Eq. (15) for calculating foF2 using the CCIR coefficient.

$$foF2(\phi,\theta,t) = a_0(\phi,\theta) + \sum_{i=1}^{M}\left[a_{2i-1}(\phi,\theta)\cos(it) + a_{2i}(\phi,\theta)\sin(it)\right] \tag{13}$$

$$a_i(\phi,\theta) = \sum_{J=0}^{j(0)} c_{i,j,0}\,P_{j,0}(\phi,\theta) + \sum_{k=1}^{9}\sum_{j=0}^{J(k)} c_{i,j,2k-1}\cos(k\phi) + c_{i,j,2k}\sin(k\phi)\sin^{j}\left(\mu(\phi,\theta)\right)\cos^{k}(\phi) \tag{14}$$

$$\mu = \arctan\left(\frac{I(\phi,\theta)}{\cos(\phi,\theta)}\right) \tag{15}$$

Where,
ϕ: North latitude;
θ: longitude;
μ: The modified dip angle;
$I(\phi,\theta)$: Earth's magnetic inclination;
$t = \pi UT/12 - \pi$, where UT is the universal time decimal hour of the day;
$J(k)$: [11, 11, 8, 4, 1, 0, 0, 0, 0].

The Neustrelitz Peak Density Model (NPDM) was proposed by Hoque and Jakowski in 2011 to provide a global empirical prediction of the peak electron density of the F2 layer (NmF2) for radio systems. The model is based on

nearly 60 years of historical data from GNSS radio occultation observations (CHAMP, GRACE, COSMIC satellites) and 177 ionospheric altimeter stations around the world, and is applicable to the average ionospheric behavior under geostatic magnetic conditions (Kp ≤ 3) [31].

The formula for NPDM calculate $NmF2$ is shown in Eq. (16) Since $NmF2$ and $foF2$ can be converted into each other, this model is used for indirect prediction.

$$NmF2 = F_1F_2F_3F_4F_5 \tag{16}$$

F_1: The variation with local time (LT in hours) is split into diurnal (D), semi-diurnal (SD) and ter-diurnal (TD) harmonic components. The model function describing the local time variation is given by F_1;
F_2: The seasonal variation of NmF2 is modeled by two components: the annual (A) and the semi-annual (SA) variation by F_2;
F_3: The geomagnetic field dependency is given by F_3;
F_4: The two ionization crests are modeled by F_4;
F_5: The strong solar activity dependence of the NmF2 is formulated by F_5.

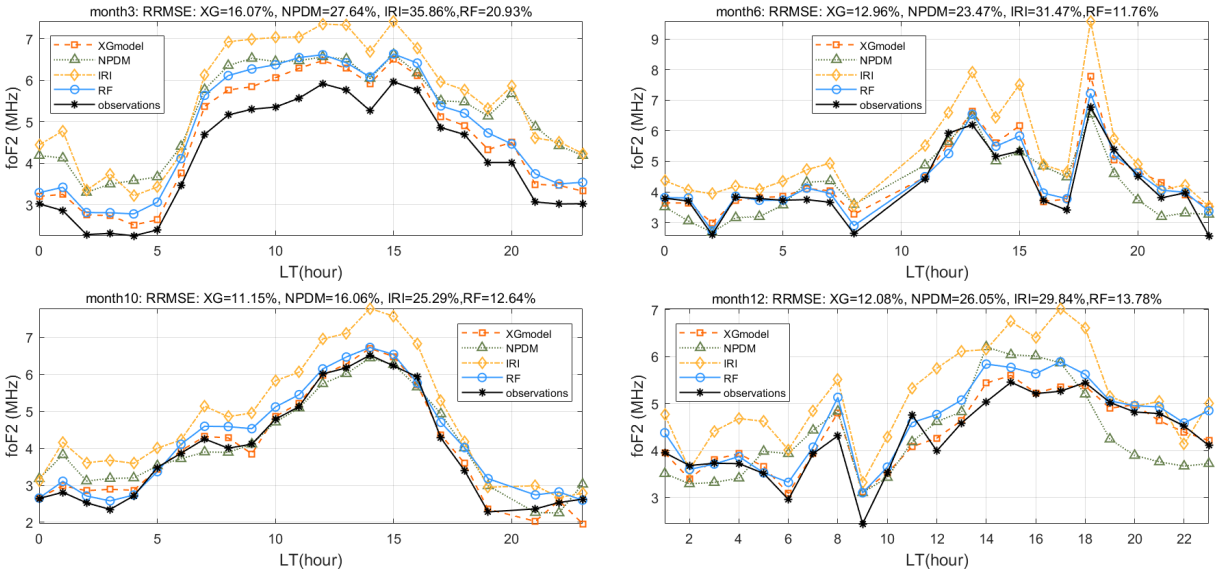

Figure 6. Changes in forecast errors and LT for March, June, October, and December 2019 using XGmodel, IRI, NPDM, and RF.

In 2019, which was a period of low solar activity, the diurnal variation of the ionospheric foF2 exhibited significant seasonal differences. As shown in Fig. 6, in the comparison of foF2 model predictions, the XGmodel demonstrated the best performance. Its relative root mean square error (RRMSE) was consistently lower than the IRI, NPDM model, and Random Forest (RF) model across all months of the year. Moreover, it showed a notable advantage in seasonal stability, with a more balanced distribution of positive and negative biases and no significant bias. In contrast, other models showed obvious shortcomings: the IRI model significantly overestimated foF2, the NPDM model had a large deviation scatter with irregular fluctuations, and the RF model had the worst performance with high errors across all seasons. Overall, the XGmodel exhibited stronger environmental adaptability and optimal predictive performance across all seasons for foF2 prediction during years of low solar activity.

This study compares the performance of four models – XGmodel, IRI-2020, RF, and NPDM – in predicting the key global ionospheric parameter foF2 for 2014 and 2019. The results show that the XGmodel, based on the XGBoost algorithm, significantly outperforms IRI-2020, NPDM, and the RF models across various evaluation metrics. In 2014, during the solar maximum, the XGmodel demonstrated exceptional predictive capability, with an R^2 of 0.88, an RMSE

of 0.98 MHz, and an MAE of 0.74 MHz – approximately 30% more accurate than the other models. The density scatter plot in Fig. 7 illustrates that the Godel's predicted and observed values form a narrow, continuous high-density band within the 5~15 MHz range. The rapid decay of the color gradient indicates the model's precision and consistency over the entire value range. This strong performance is attributed to XGmodel's ability to efficiently capture complex nonlinear relationships in the ionosphere and its optimized feature engineering.

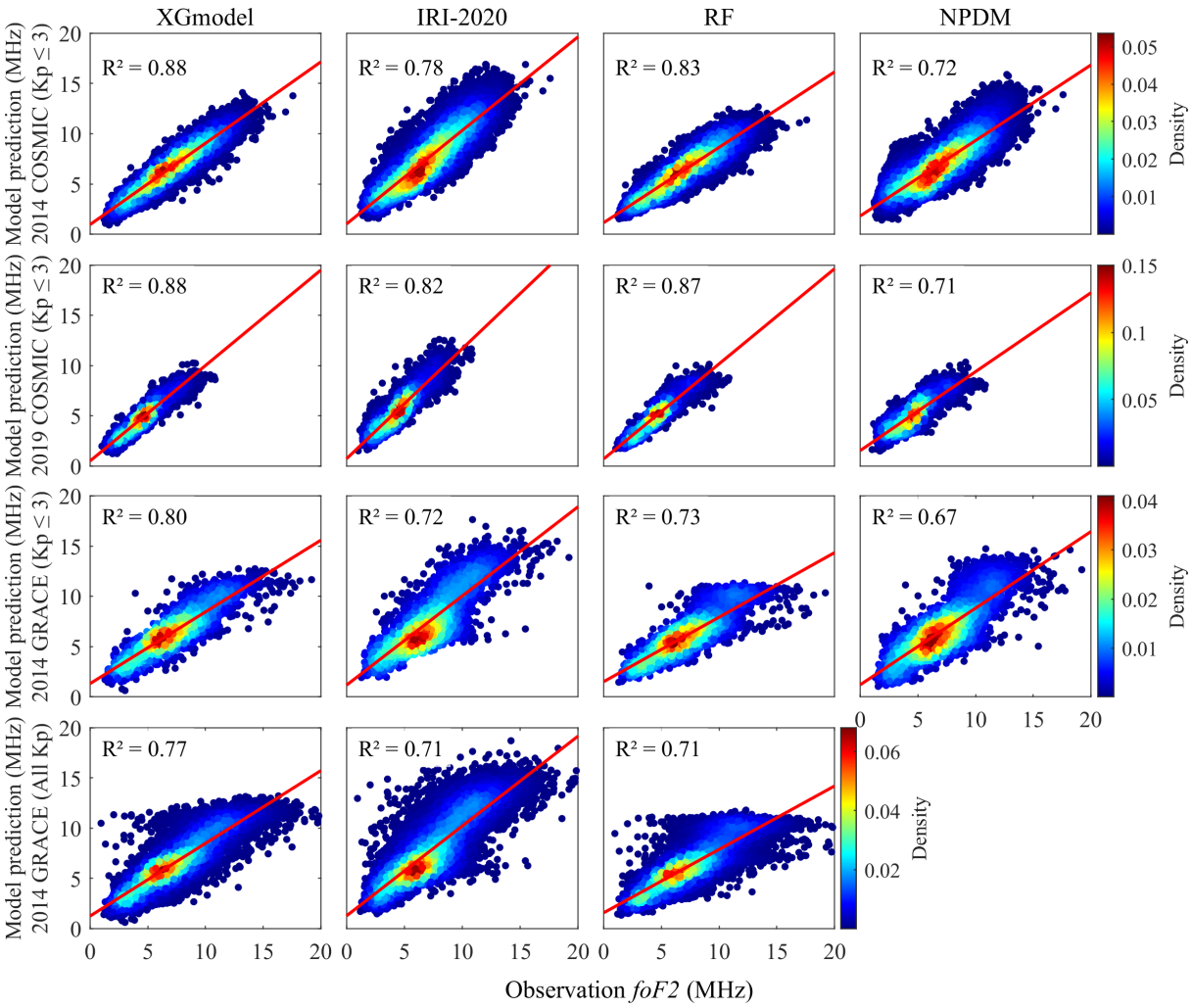

Figure 7. Scatter plots of the XGmodel, IRI-2020, RF, and NPDM models' accuracy in predicting geomagnetic (Kp ≤ 3) and under all geomagnetic conditions, using COSMIC satellite foF2 measurements from 2014 and 2019, and GRACE satellite foF2 measurements from 2014 as benchmarks. (The NPDM model is applicable only to Kp ≤ 3, so only data with Kp ≤ 3 are used to compare the accuracy of NPDM model predictions).

During the 2019 solar minimum, the XGmodel maintained its strong generalization capabilities, with an R^2 of 0.88. The error metrics improved further, with RMSE reduced to 0.62 MHz and MAE to 0.47 MHz, meeting the accuracy requirements for engineering applications.

To assess the model's robustness under different data sources, we validated the XGmodel using data from seven GRACE satellite observation sites and the GIRO ground station. The results, presented in Table 3, show that while the performance of all models slightly declined under conditions of Kp ≤ 3, the XGmodel continued to outperform IRI-2020, RF, and NPDM. Its density scatter plot displayed a significant high-density, elongated distribution, confirming its superior data fitting accuracy. Under the Kp = All condition, the R^2 values for XGmodel, IRI-2020, and NPDM decreased by 0.03, 0.01, and 0.02, respectively, but remained stable. The XGmodel's density scatter plot continued to show a more concentrated high-density region, validating its robustness across different geomagnetic conditions.

Using independent validation data from seven representative GIRO sites worldwide in 2019 (Fig. 8), which span high, mid, and low latitudes in both hemispheres as well as the equatorial region, we evaluated the foF2 prediction accuracy of the XGmodel, IRI-2020, RF, and NPDM models (see Table 3). The results show that XGmodel achieves the best overall performance across most regions. Among the seven sites, XGmodel attains the highest R^2 at five locations, particularly in the equatorial region, low-latitude Southern Hemisphere, and high-latitude Northern Hemisphere. Furthermore, in mid-to-high latitude regions, XGmodel's prediction errors are substantially lower than those of IRI-2020 and NPDM, with improvements generally exceeding 50%. The only exception is the high-latitude Southern Hemisphere, where NPDM shows slightly lower RMSE and MAE than XGmodel, although XGmodel still maintains a higher R^2 than IRI-2020.

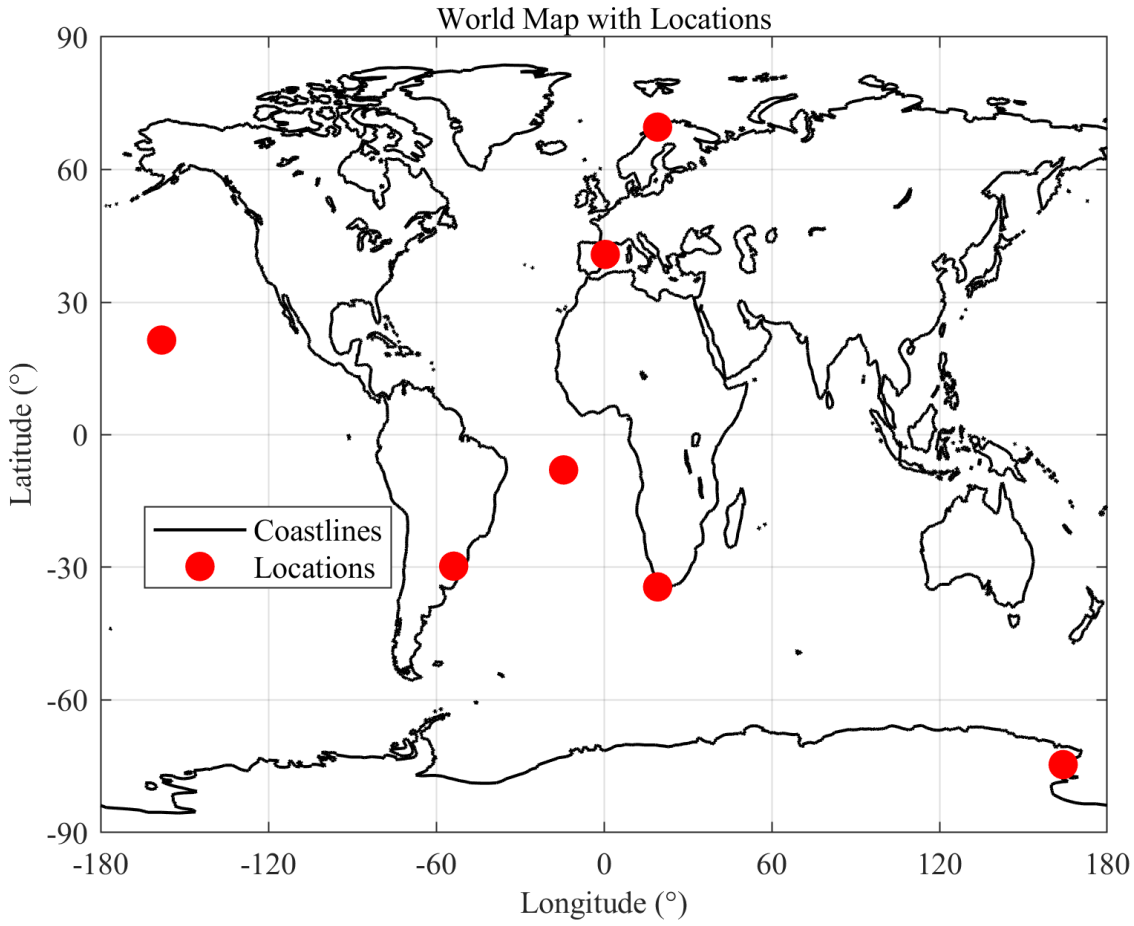

Figure 8. Distribution of ionosonde stations, where the red dots are vertical measurement sites.

To visually compare the overall performance of different models, this study used a Taylor diagram to analyze the prediction results of each model in Table 3, based on the GIRO representative sites, 2014 COSMIC, 2019 COSMIC, and 2014 GRACE data as benchmarks, as shown in Fig. 9. The Taylor diagram displays three key statistical metrics: correlation coefficient (R), standard deviation ratio (σ), and centralized root mean square error (CRMSE). In the diagram, the normalized standard deviation of the observed values (1.0) serves as the reference arc. The closer a model's point is to this arc and the higher its correlation coefficient, the better its overall performance. The analysis shows that the XGmodel is closest to the observed values across all datasets, demonstrating the best overall performance.

Comprehensive multi-dimensional evaluation shows that the XGmodel based on data-driven and machine learning algorithms is superior to traditional empirical models and RF in prediction accuracy, consistency, value range coverage and generalization ability. In particular, it shows unique advantages in dealing with nonlinear responses and extreme values of ionospheric parameters and has significant potential for engineering applications.

Table 3. The four models, XGmodel, IRI-2020, RF, and NPDM, use the COSMIC satellite foF2 measurement data with kp ≤ 3 in 2014 and 2019, the GRACE satellite in 2014, and the GIRO seven stations in 2019 as the benchmarks to predict the evaluation parameters under the conditions of Kp ≤ 3 and Kp = All (because the NPDM model is only applicable to the geomagnetic conditions with kp ≤ 3, the data with kp ≤ 3 are selected for comparison).

Data sorce	Year	Model	R^2	RMSE (MHz)	MAE (MHz)
COSMIC-1	2014 (kp ≤ 3)	XGmodel	0.88	0.98	0.74
		IRI-2020 (STORM)	0.78	1.39	1.07
		NPDM	0.72	1.38	1.07
		RF	0.83	1.23	0.91
	2019 (kp ≤ 3)	XGmodel	0.88	0.62	0.47
		IRI-2020 (STORM)	0.82	1.43	1.18
		NPDM	0.71	1.02	0.81
		RF	0.87	0.74	0.59
GRACE	2014 (kp ≤ 3)	XGmodel	0.80	1.57	1.13
		IRI-2020 (STORM)	0.72	1.73	1.31
		NPDM	0.67	1.82	1.38
		RF	0.73	1.92	1.39
	2014	XGmodel	0.77	1.63	1.19
		IRI-2020 (STORM)	0.71	1.79	1.32
		RF	0.71	1.98	1.45
GIRO lat = −7.95 lon = −14.40	2019 (kp ≤ 3)	XGmodel	0.88	1.44	1.13
		IRI-2020 (STORM)	0.81	2.77	2.43
		NPDM	0.74	2.85	2.65
		RF	0.78	2.29	2.05
GIRO lat = 21.43 lon = −158.15	2019 (kp ≤ 3)	XGmodel	0.72	1.76	1.29
		IRI-2020 (STORM)	0.77	3.08	2.79
		NPDM	0.57	2.94	2.67
		RF	0.61	5.31	4.69

Data sorce	Year	Model	R^2	RMSE (MHz)	MAE (MHz)
GIRO lat = −29.73 lon = −53.71	2019 (kp ≤ 3)	XGmodel	0.81	1.78	1.34
		IRI-2020 (STORM)	0.75	2.71	2.35
		NPDM	0.55	3.28	2.73
		RF	0.49	3.00	2.43
GIRO lat = 40.80 lon = 0.50	2019 (kp ≤ 3)	XGmodel	0.82	0.59	0.40
		IRI-2020 (STORM)	0.81	2.65	2.58
		NPDM	0.54	2.15	2.01
		RF	0.22	2.46	2.21
GIRO lat = −34.42 lon = 19.22	2019 (kp ≤ 3)	XGmodel	0.84	0.71	0.53
		IRI-2020 (STORM)	0.88	2.50	2.41
		NPDM	0.73	2.18	2.01
		RF	0.48	2.48	2.17
GIRO lat = 69.60 lon = 19.20	2019 (kp ≤ 3)	XGmodel	0.74	0.37	0.29
		IRI-2020 (STORM)	0.69	2.36	2.32
		NPDM	0.40	2.19	2.12
		RF	0.39	2.26	2.13
GIRO lat = −74.62 lon = 164.24	2019 (kp ≤ 3)	XGmodel	0.52	0.74	0.52
		IRI-2020 (STORM)	0.47	2.28	2.17
		NPDM	0.52	1.51	1.37
		RF	0.27	2.05	1.80

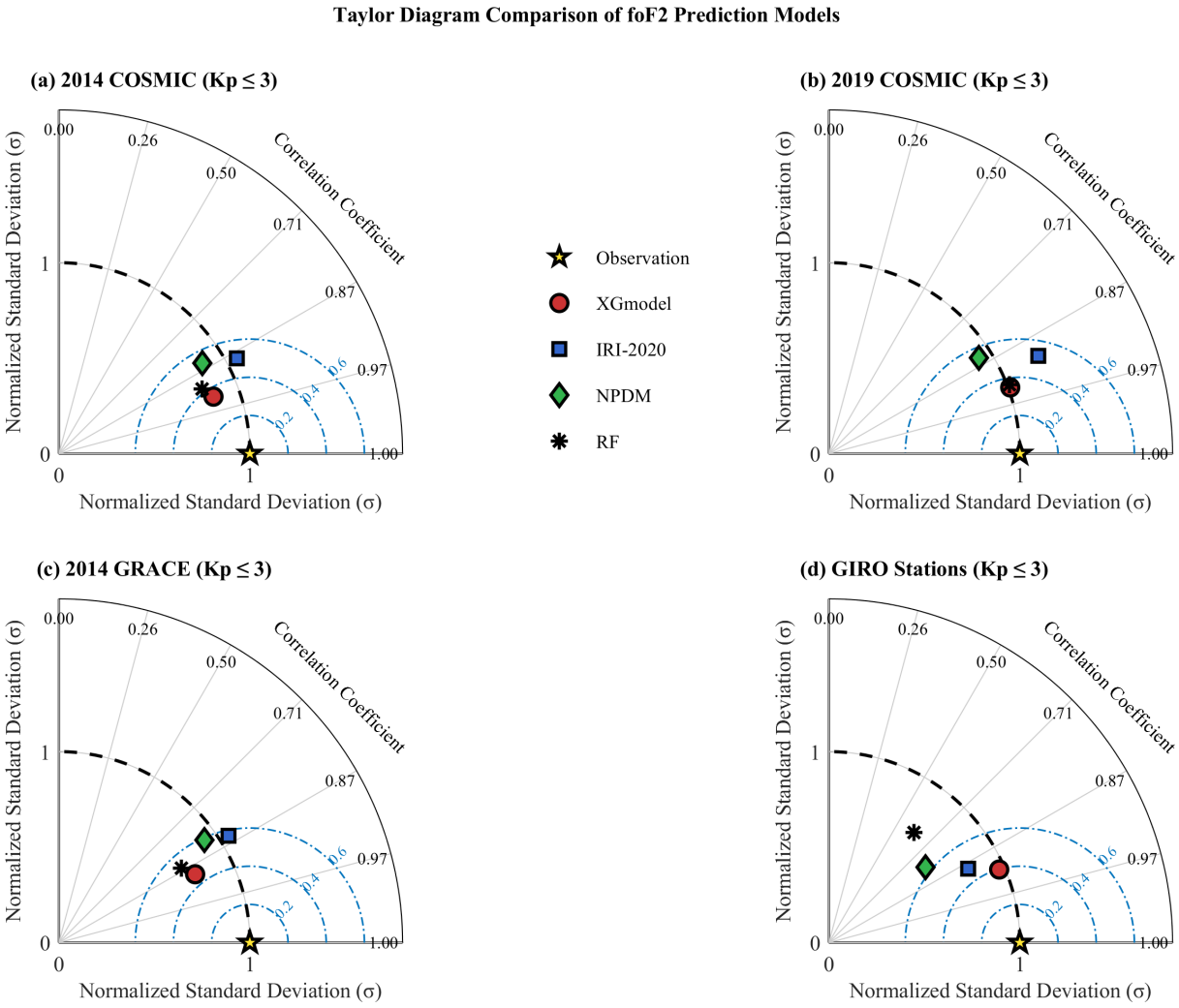

Figure 9. Taylor Diagrams of foF2 Predicted by XGmodel, IRI-2020, NPDM, and RF Models Against COSMIC 2014, COSMIC 2019, and GRACE 2014 Measurements (for Kp ≤ 3 and GRACE 2014 Kp = All Scenarios).

5. Analysis and Interpretability of Modeling and Prediction Performance

5.1 Analysis of the Effect of COSMIC-2 Data on Improving Modeling and Prediction Accuracy in Low-latitude Regions

The COSMIC-1 satellite provides valid data across the latitude range of −89.94° to 89.97°, while the COSMIC-2 satellite covers a more limited range of −42.55° to 42.91°, focusing on low-latitude regions. The dataset includes 6,805,448 valid data points, with 4,235,328 (62.23%) originating from the COSMIC-2 satellite. Incorporating COSMIC-2 data reduces the MAE and RMSE for low-latitude areas by 2.39% and 2.63%, respectively, significantly enhancing forecast accuracy.

Table 4. Training results before and after adding COSMIC-2 to the dataset.

Data composition	MAE (MHz)	RMSE (MHz)
COSMIC-1, COSMIC-2	0.773	1.015
COSMIC-1	0.792	1.042

Table 5. Compares the foF2 predictions for low-latitude regions in 2014, a year of high solar activity, using the XGmodel, IRI-2020, NPDM and RF models. The RMSE and MAE of the XGmodel are 36.3% and 38.9% lower than those of the IRI-2020 and 32.0% and 35.8% lower than those of the NPDM. These low errors indicate that the XGmodel has greater predictive stability in low-latitude regions.

Model	R^2	RMSE (MHz)	MAE (MHz)
XGmodel	0.89	1.02	0.77
IRI-2020	0.80	1.60	1.26
NPDM	0.72	1.50	1.20
RF	0.80	1.45	1.10

5.2 Interpretability Analysis

To estimate the expected prediction value when features are missing, the XGmodel training data is used as the baseline distribution. This study uses a random sampling strategy: 10,000 samples are drawn from the training set to construct the baseline distribution, and 3,000 samples are selected from the test set to calculate the SHAP value.

In Fig. 10a is a feature importance ranking diagram, and Fig. 10b is a bee swarm diagram. The horizontal axis in Fig. 10a represents the average absolute SHAP value, the horizontal axis in Fig. 10b represents the SHAP value, and the vertical axis is the global feature importance ranking. The color mapping reflects the size of the feature value, blue represents low value, and red represents high value.

The feature importance ranking based on the average SHAP absolute value shows that local time (LT), latitude (Lat), solar radiation index (F10.7), day of year (Doy) and year (year) are the top five key driving factors, and their contribution magnitude is significantly higher than that of other features. The average absolute SHAP value of local

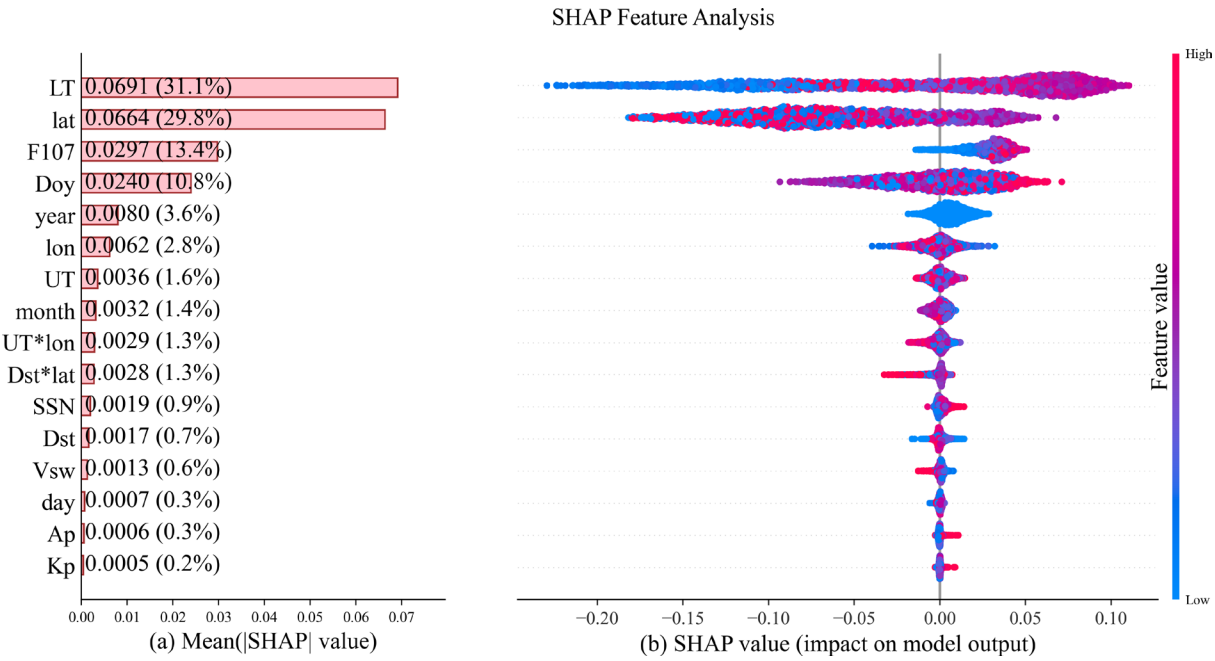

Figure 10. Feature Importance Analysis (a) Bar chart on the left: Average absolute SHAP value of features and their relative contribution percentages; (b) Beeswarm plot on the right: SHAP value distribution, with the color of the dots indicating the feature value. Features are sorted in descending order of importance.

time (LT) ranks first among all variables, contributing 31.1% to the critical frequency prediction, making it the most critical factor affecting model prediction.

LT was identified as the most influential feature, and its effect showed significant hemispheric differences: the SHAP values of samples at high latitudes ($|Lat| > 50°$) were generally negative and large in absolute value, indicating that it had a downward effect on the foF2 prediction, which may be related to the enhancement of ionospheric cavitation and particle precipitation in the polar regions (Paulikas, 1971; Muralikrishna, 2003). Year, as a proxy variable representing the solar activity cycle, has a wider distribution of SHAP values in the solar high year (2014), with SHAP $\in [0.04, 0.09]$, while the low year (2019) is concentrated in a smaller range, with SHAP $\in [0.05, 0.075]$, reflecting that the model effectively captures the modulation effect of the solar activity cycle (Usoskin, 2021).The SHAP value of the solar radiation index (F10.7) is generally positive within the normal activity level ($F10.7 < 200$ sfu), which is highly consistent with the physical mechanism of F10.7 as the main ionization source of the ionosphere (Liu, 2006; Balan, 1995). The enhancement of solar extreme ultraviolet (EUV) radiation directly leads to the increase of ionospheric electron density. Doy and Lon have similar effects on the increase and decrease of foF2, with nonlinear effects. This difference caused by longitude may be related to the ionospheric asymmetry caused by the geomagnetic field bias effect (Aa, 2019). The SHAP values of other parameters are very small, indicating that these parameters have relatively limited influence on the model prediction.

To verify whether the interpretability analysis of SHAP values calculated from samples of training and test sets has the ability to generalize to data from other sources, a dataset consisting of GRACE satellite data was used to calculate SHAP values. The results showed that the top five important variables were local time (LT), latitude (Lat), annual days (Doy), solar radiation index (F10.7), and longitude (Lon).

Notably, all core physical features (Lat, LT, F10.7 and Doy) remained in the top five in both datasets. Latitude, the most important spatial feature, ranked in the top two in both datasets, and F10.7 held the same ranking. These findings demonstrate that the core explanatory mechanism of the XGboost model possesses robust generalization capabilities, unaffected by data temporal range, source differences, or sampling ratio.

To verify the reliability of the feature importance ranking method based on SHAP values, this study conducted a feature ablation experiment, comparing the performance of an XGBoost model built using the full feature set of 16 variables with a subset of the top six key features ranked by SHAP values. The experimental results, shown in Table 6, show only a slight decrease in model performance when the feature dimension is reduced by 62.5%. Compared with the baseline full-feature model, the model constructed with the key feature subset has a decrease in coefficient of determination of 0.038, an increase in RMSE of 0.102 MHz, and an increase in MAE of 0.060 MHz; while the key feature subset model still maintains a core prediction accuracy above 0.85.

This result demonstrates that the SHAP method can effectively select the subset of features that plays a decisive role in foF2 prediction. While maintaining the core prediction accuracy of the model, a significant reduction in feature dimensionality did not lead to a significant performance degradation, thus validating the reliability of the SHAP feature ranking method. Furthermore, this research finding provides a quantitative basis for the physical interpretation of ionospheric influencing factors in the XGBoost model, contributing to a deeper understanding of the mechanisms by which these influencing factors affect ionospheric parameter prediction.

Table 6. Comparative analysis of prediction accuracy of XGmodel with reduced core training features.

	R^2	RMSE (MHz)	MAE (MHz)
Critical Subset Model	0.848	1.066	0.784
Baseline model	0.886	0.964	0.724
Variation	−0.038	+0.102	+0.060

It should be noted that certain input features are physically or statistically correlated, leading to redundancy. Temporal redundancy exists among Month, Day, DOY, UT, and LT. Solar activity proxies F10.7 and SSN are highly correlated, and geomagnetic indices Kp and Ap are mathematically related. Such redundancy may cause SHAP

value dilution, where the contribution of a feature is distributed across its correlated counterparts, potentially underestimating its actual importance. In this study, dominant features including LT, Lat, and F10.7 remain stable as core drivers, whereas some lower-ranked features may appear less important primarily due to correlation-induced dilution rather than negligible physical influence.

6. Summary

This study constructed a global ionospheric critical frequency (foF2) prediction model, XGmodel, based on the XGBoost algorithm. It was trained and evaluated using COSMIC occultation data. The results demonstrate that XGmodel has excellent predictive capabilities, with an R2 of 0.886 and an RMSE of 0.964 MHz. Specific findings are as follows:

The model successfully reproduces key ionospheric structures, including the EIA, the Weddell Sea anomaly, and the ionospheric winter anomaly.

The comparison of GRACE and vertical survey data shows that XGmodel exhibits excellent generalization ability. In 2014, its R^2 is 0.80 ($kp \leq 3$) and 0.77, RMSE is 1.57 and 1.63, and MAE is 1.13 and 1.19. In 2019, the R^2 is the highest at 0.88, the RMSE is the lowest at 0.37, and the MAE is the lowest at 0.29 in the multi-GIRO site scenario (all $kp \leq 3$). The key indicators are stable and the performance is outstanding.

After integrating COSMIC-2 data, the prediction accuracy of the model in low-latitude areas is further improved, with MAE and RMSE reduced by 2.39% and 2.63% respectively.

Through SHAP interpretability analysis, the five core physical features driving global foF2 predictions were quantitatively revealed for the first time, with their importance ranking being highly consistent across different datasets. Feature ablation experiments demonstrated that only 37.5% of the key features were required to maintain core prediction accuracy, significantly enhancing the model's lightweight potential and physical interpretability. This also validated the model's successful capture of physical mechanisms such as solar cycle modulation and hemispheric asymmetry.

Data availability statement. Data can be downloaded at: https://data.cosmic.ucar.edu/gnss-ro/. https://omniweb.gsfc.nasa.gov/form/dx1.html.

Acknowledgements. I sincerely express my gratitude to my teacher, Professor Ou Ming, for his invaluable assistance and guidance in thesis topic selection, experimental methodology, and manuscript writing, and for his contribution to writing – review and editing, as well as supervision and funding acquisition. I also owe special thanks to my senior fellow student, Zhang Yuhang, for his meticulous review and constructive comments on the thesis revision, particularly in the aspect of writing – review and editing. Additionally, I acknowledge the contributions of all other authors: Q.L.Z. and J.L. carried out validation, with Q.L.Z. also managing project administration; J.C. performed formal analysis; R.C. conducted investigation; H.Z. and J.L. provided resources; Q.Z. took charge of visualization.

References

Aa, E., S. Zou, A. J. Ridley, S. Zhang et al. (2019). Merging of storm time midlatitude traveling ionospheric disturbances and equatorial plasma bubbles, Space Weather, 17, 285-298, doi:10.1029/2018SW002101.

Balan, N. and G. J. Bailey (1995). Equatorial plasma fountain and its effects: Possibility of an additional layer, J. Geophys. Res. Space Phys., 100, A11, 21421-21432, doi:10.1029/95JA01555.

Bilitza, D., D. Altadill, V. Truhlik, V. Shubin et al. (2017). International Reference Ionosphere 2016: From ionospheric climate to real-time weather predictions, Space Weather, 15, 2, 418-429, doi:10.1002/2016SW001593.

Bi, C., P. Ren, T. Yin, Z. Xiang et al. (2022). Modeling and forecasting ionospheric foF2 variation in the low latitude region during low and high solar activity years, Remote Sens., 14, 21, 5418, doi:10.3390/rs14215418.

Breiman, L. (2001). Random forests, Mach. Learn., 45, 1, 5-32, doi:10.1023/A:1010933404324.

Chen, T. and C. Guestrin (2016). Xgboost: A scalable tree boosting system, In Proc. 22nd ACM SIGKDD, Int. Conf. Knowl. Discov. Data Min., 785-794, doi:10.1145/2939672.2939785.

Cohen, J., X. Huan and J. Ni (2024). Shapley-based explainable ai for clustering applications in fault diagnosis and prognosis, J. Intell. Manuf., 35, 1013-1028, doi:10.1007/s10845-024-02468-2.

Forsythe, V. V., D. Bilitza, A. G. Burrell, K. F. Dymond et al. (2024). PyIRI: Whole-globe approach to the International Reference Ionosphere modeling implemented in Python, Space Weather, 22, e2023SW003739, doi:10.1029/2023SW003739.

Gowtam, V. S. and S. T. Ram (2017). Ionospheric winter anomaly and annual anomaly observed from Formosat-3/COSMIC Radio Occultation observations during the ascending phase of solar cycle 24, Adv. Space Res., 60, 8, 1585-1593, doi:10.1016/j.asr.2017.03.017.

Habarulema, J. B., L. A. McKinnell, P. J. Cilliers and B. D. L. Opperman (2009). Application of neural networks to South African GPS TEC modelling, Adv. Space Res., 43, 11, 1711-1720, doi:10.1016/j.asr.2008.08.020.

Han, C., P. Gang, J. Ruimin, Z. Weimin et al. (2024). Characterization of topside ionospheric scale height based on COSMIC occultation observations, Chin. J. Radio Sci., 39, 2, 253-261, doi:10.12265/j.cjors.2023060.

Joseph, O. O., Y. Yamazak, P. Cilliers, P. Baki et al. (2015). A study on the response of the equatorial ionization anomaly over the East Africa sector during the geomagnetic storm of November 13, 2012, Adv. Space Res., 55, 12, 2863-2872, doi:10.1016/j.asr.2015.03.011.

Li, X., C. Zhou, Q. Tang, J. Zhao et al. (2021). Forecasting ionospheric foF2 based on deep learning method, Remote Sens., 13, 19, 3849, doi:10.3390/rs13193849.

Lin, M., X. Zhu, T. Hua, X. Tang et al. (2021). Detection of ionospheric scintillation based on XGBoost Model Improved by SMOTE-ENN Technique, Remote Sens., 13, 13, 2577, doi:10.3390/rs13132577.

Liu, L., W. Wan, B. Ning, O. M. Pirog et al. (2006). Solar activity variations of the ionospheric peak electron density, J. Geophys. Res. Space Phys., 111, A8, doi:10.1029/2006JA011598.

Lundberg, S. M. and S. I. Lee (2017). A unified approach to interpreting model predictions, Adv. Neural Inf. Process. Syst., 30, 1-15, doi:10.48550/arXiv.1705.07874.

Lundberg, S. M., G. G. Erion and S. I. Lee (2018). Consistent individualized feature attribution for tree ensembles, arXiv preprint, arXiv 1802.03888, doi:10.48550/arXiv.1802.03888.

Lundberg, S. M., B. Nair, M. S. Vavilala, M. Horibe et al. (2018). Explainable machine-learning predictions for the prevention of hypoxaemia during surgery, Nat. Biomed. Eng., 2, 10, 749-760, doi:10.1038/s41551-018-0304-0.

Muralikrishna, P., L. P. Vieira and M. A. Abdu (2003). Electron density and electric field fluctuations associated with developing plasma bubbles, J. Atmos. Sol. Terr. Phys., 65, 14-15, 1315-1327, doi:10.1016/j.jastp.2003.08.010.

Paulikas, G. A. (1971). The patterns and sources of high-latitude particle precipitation, Rev. Geophys., 9, 3, 659-701, doi:10.1029/RG009i003p00659.

Pezzopane, M. and C. Scotto (2007). Automatic scaling of critical frequency foF2 and MUF(3000)F2: A comparison between Autoscala and ARTIST 4.5 on Rome data, Radio Sci., 42, 4, RS4008, doi:10.1029/2006RS003581.

Qian, L., A. G. Burns, B. A. Emery, B. Foste et al. (2014). The NCAR TIE-GCM: A community model of the coupled thermosphere-ionosphere system, Modeling the Ionosphere-Thermosphere System, 73-83, doi:10.1002/9781118704417.ch7.

Qiao, F., Z. Y. Xing, Q. H. Zhang, H. B. Zhang et al. (2024). A long time-series forecasting informer architecture-based ionospheric foF2 model in the low-latitude region, Front. Astron. Space Sci., 11, 1418918, doi:10.3389/fspas.2024.1418918.

Shi, Y., C. Jang, J. Wang and F. Meng (2025). A hybrid deep learning-based short-term forecast model for ionospheric foF2 in East Asia region, Adv. Space Res., 75, 1, 988-1002, doi:10.1016/j.asr.2024.09.062.

Usoskin, I. G., S. K. Solanki, N. A. Krivova, B. Hofer et al. (2021). Solar cyclic activity over the last millennium reconstructed from annual 14C data, Astron. Astrophys., 649, A141, doi:10.1051/0004-6361/202140711e.

Vesnin, A. M., I. A. Galkin and P. Song (2015). Validation of F2 layer peak height and density by Real-Time IRI, In 1st URSI Atlantic Radio Sci. Conf., URSI AT-RASC, 1-4, doi:10.1109/URSI-AT-RASC.2015.7303202.

Wang, J., Q. Yu, Y. Shi, Y. Liu et al. (2023). An Explainable Dynamic Prediction Method for Ionospheric foF2 Based on Machine Learning, Remote Sens., 15, 5, 1256, doi:10.3390/rs15051256.

Wang, N., Y. Yuan, Z. Li and X Huo (2016). Improvement of Klobuchar model for GNSS single-frequency ionospheric delay corrections, Adv. Space Res., 57, 7, 1555-1569, doi:10.1016/j.asr.2016.01.010.

Zhao, J., B. Ren, F. Wu, H. Liu et al. (2023). TECX-TCN: Prediction of ionospheric total electron content at different latitudes in China based on XGBoost algorithm and temporal convolution network, J. Atmos. Sol. Terr. Phys., 249, 106091, doi:10.1016/j.jastp.2023.106091.

Zewdie, G. K., C. Valladares, M. B. Cohen, D. L. Lary et al. (2021). Data-driven forecasting of low-latitude ionospheric total electron content using the random forest and LSTM machine learning methods, Space Weather, 19, 4, e2020SW002639, doi:10.1029/2020SW002639.

***CORRESPONDING AUTHOR: Ming OU**,
Shandong University of Science and Technology, Department of Ocean Science and Engineering, 266000 Qing Dao, China
e-mail: ohm1122@163.com